NMDAR-dependent supralinear dendritic integration in murine neurogliaform interneurons

Authors and affiliations

Simonas Griesius[1], Dimitri M Kullmann[1]*

[1]Department of Clinical Experimental and Epilepsy, UCL Queen Square Institute of Neurology,

University College London, London, WC1N 3BG, United Kingdom

*Corresponding author

Running title

Supralinear dendritic integration in interneurons

Keywords

Calcium imaging, nonlinear summation, synaptic plasticity, L-type calcium channel, credit assignment,

Acknowledgements

We thank all members of the Kullmann lab and the wider Department of Clinical and Experimental Epilepsy for contributing to discussions surrounding the presented work.

Funding

The authors gratefully acknowledge support from the Wellcome Trust (212285/Z/18/Z). We thank Amy Richardson for the development of the virus used to drive reporter expression.

Conflict of interest

The authors declare no conflicts of interest.

Abstract

Non-linear summation of synaptic inputs to the dendrites of pyramidal neurons has been proposed to increase the computation capacity of neurons through coincidence detection, signal amplification, and additional logic operations such as XOR. Supralinear dendritic integration has been documented extensively in principal neurons, mediated by several voltage-dependent conductances. It has also been reported in parvalbumin-positive hippocampal basket cells, although only in dendrites innervated by feedback excitatory synapses. Whether other interneurons, which exclusively support feed-forward inhibition of principal neurons, also exhibit local non-linear integration of synaptic excitation is not known. Here we use patch-clamp electrophysiology, and 2-photon calcium imaging and glutamate uncaging, to show that supralinear dendritic integration of near-synchronous spatially clustered glutamate-receptor mediated depolarization occurs in NDNF-positive neurogliaform cells in the mouse hippocampus. Supralinear summation was detected via recordings of somatic depolarizations elicited by near-synchronous uncaging of glutamate on dendritic fragments, and concurrent imaging of dendritic calcium transients. Supralinearity was abolished by blocking NMDA receptors (NMDARs) but resisted blockade of voltage-gated sodium channels. Blocking L-type calcium channels abolished supralinear calcium signalling but only had a minor effect on voltage supralinearity. Dendritic boosting of spatially clustered synaptic signals argues for previously unappreciated computational complexity in neurogliaform cells.

Introduction

Accumulating evidence indicates that dendrites do more than merely summate excitatory and inhibitory synaptic inputs[1-6]. Dendrites endow neurons with increased computational capacity[7] and the ability to act as multi-level hierarchical networks[8,9] or even to reproduce some features of artificial and deep neural networks[10,11]. The underlying mechanisms include extensive dendritic arborisation, compartmentalisation, synaptic plasticity and expression of specific receptors and ion channels that in turn facilitate nonlinear input summation. Nonlinear dendritic integration of excitatory inputs in particular can potentially support signal amplification[12], coincidence detection[13], XOR logic gating[14,15], and computing prediction errors[2,11]. One striking example of non-linear integration is local supralinear summation of signals that arrive at a dendritic fragment in a narrow time window, a phenomenon that can be investigated by exploiting the spatial and temporal precision of somatic depolarizations elicited by multi-photon glutamate uncaging[16-21]. Several receptors and channels have been implicated in supralinear summation in principal neurons, including NMDARs[16-19,21-27], calcium-permeable AMPARs[21,25,26], and voltage-gated sodium channels[20,21,24,25,27,28], calcium channels[19,21,25,27], and potassium channels[29,30]

Inhibitory interneurons have a crucial role in brain circuit and network excitability, rhythmicity, and computations[31-33]. However, in comparison with principal cells, relatively little is known about non-linear dendritic integration in interneurons. Katona et al. (2011) reported NMDAR-dependent supralinearly summating EPSPs recorded at the soma and calcium transients in the dendrites of CA1 interneurons, although these were not identified using molecular or genetic markers[18]. Chiovini et al. (2014) subsequently reported supralinearly summating EPSPs and dendritic calcium transients in parvalbumin-positive (PV+) interneurons[21], and Camire and Topolnik (2014) and Camire et al. (2018) reported supralinearly summating dendritic calcium transients in the same cell type[25,26]. Using multiphoton glutamate uncaging, Cornford et al. (2019) also showed evidence for NMDAR-dependent supralinear EPSP summation in PV+ basket cells, although this was only seen in dendrites receiving feedback excitation in stratum oriens and not in dendrites receiving feed-forward excitation in stratum radiatum[16]. Failure to detect supralinear summation in stratum radiatum dendrites of PV+ interneurons is consistent with evidence from dendritic recordings that somatic action potentials attenuate rapidly as they back-propagate, and that PV+ dendrites express abundant Kv3 family potassium channels and relatively few sodium channels[34]. Indeed, compartmental modelling has been used to infer that synaptic inputs to PV+ interneuron dendrites summate sublinearly, and that this helps to ensure that they do not disrupt population spike synchrony during gamma oscillations[35]. In contrast to the evidence for both supra- and sublinear summation in PV+ interneurons (likely to occur simultaneously in different dendrites)[16], it remains unknown how synaptic inputs are integrated in other forebrain interneurons. As for other brain regions, cerebellar cortex stellate cells have been shown to exhibit sublinear summation of uncaging-evoked EPSPs whilst simultaneously exhibiting supralinear summation of dendritic calcium transients[19].

Dysfunction of interneurons generally has been associated with a variety of psychiatric and neurological pathologies, including epilepsy[36-39], schizophrenia [40-42], autism spectrum disorder[42,43] and Alzheimer's diease[44,45], among others[46]. There is emerging evidence suggesting that impairments in dendritic

integration[20,47-50], and specifically in interneurons[20], may be important contributors to pathological phenotypes in psychiatric and neurological pathologies. We therefore set out to characterize dendritic integration in PV-negative neurogliaform interneurons, which support feed-forward inhibition of the apical dendrites of CA1 pyramidal neurons. Neurogliaform cells can be identified in stratum lacunosum-moleculare (SLM) using knock-in mice expressing cre recombinase at the neuron-derived neurotrophic factor (NDNF) locus[51-54], and mediate feed-forward inhibition and receive inputs from the entorhinal cortex and the nucleus reuniens[52], with distinct plasticity rules at synapses made by these afferents[53].

We quantified non-linear dendritic summation using 2-photon glutamate uncaging at multiple locations within a small dendritic fragment, by comparing the arithmetic sum of the uncaging-evoked EPSPs evoked individually to the result of near-synchronous glutamate uncaging[16]. We asked if neurogliaform interneurons exhibit non-linear summation and whether this depended on NMDARs or sodium or calcium channels. In parallel, we asked if non-linear summation could also be detected in these cell types by concurrent measurement of dendritic calcium-dependent fluorescence transients.

Results

NDNF-positive (NDNF+) neurogliaform interneurons were studied in the hippocampal CA1 stratum lacunosum/moleculare in acute slices from NDNF-cre mice injected with AAV2/9-mDLX-FLEX-mCherry virus (Fig 1a). In order to probe the spatiotemporal dynamics of dendritic integration, glutamate was locally delivered by 2-photon uncaging of bath-perfused MNI-glutamate (3 mM) using an infrared (720nm) pulsed laser at points along second order dendrites, whilst recording from their somata with a patch pipette. The absence of dendritic spines prevented identification of the sites of excitatory synapses, and the uncaging locations were therefore spaced 1 – 2 µm apart, either side of the selected dendritic fragment[16] (Fig. 1b, c). The locations were kept within a dendritic length of ~15 µm, consistent with the size of interneuron dendritic domains exhibiting correlated tuning of synaptic calcium transients in vivo[55]. Glutamate uncaging reliably elicited somatic uncaging EPSPs (uEPSPs) (Fig. 1d). The uncaging was performed with pulses separated by an interval of either 100.32 ms (asynchronously) or 0.32 ms, near-synchronously. The number of uncaging stimuli at neighbouring locations was cumulatively increased from 1 to 12 in the near-synchronous condition. The somatic uEPSP evoked by near-synchronous uncaging was greater in both amplitude and duration than predicted from the arithmetic sum of the individual somatic uEPSPs. Consistent with supralinear integration in principal neurons and at oriens dendrites in PV+ interneurons, as the number of uncaging sites was increased, the recorded near-synchronously evoked uEPSPs initially summated linearly, and then deviated from the line of identity upon activation of multiple uncaging locations. The supralinearity was more marked when the uEPSP was quantified by integrating the somatic depolarization for 100ms (area under the curve, AUC) than when measured as peak amplitude (Fig 1e, f), as expected from the recruitment of voltage-dependent conductances. As the number of uncaging locations was increased further, the peak amplitude showed a tendency to reach a plateau, consistent with a decrease in driving force as the local dendritic membrane potential approached the synaptic reversal potential.

In parallel with measurement of uEPSPs, we measured dendritic calcium transients by monitoring the fluorescence of the calcium sensor Fluo-4, which was included in the pipette solution, using a second pulsed infrared scanning laser tuned to 810 nm (Fig 2a). The interval between glutamate uncaging pulses in the asynchronous condition was too short to allow the dendritic Fluo-4 signal to relax to baseline in between stimuli. Instead, we examined the peak amplitude of the dendritic calcium response, either in response to asynchronous uncaging at all 12 locations (Fig. 2b) or with an increasing number of near-synchronous stimuli (Fig. 2c). In the same neurogliaform neuron illustrated in Fig. 1, this revealed a discontinuity, where the peak amplitude of the dendritic calcium fluorescence transient increased abruptly with 6 or more near-synchronous uncaging locations (Fig 2c). In order to characterize the supralinearity of the calcium transients, we interpolated the calcium response from 1 location uncaged to the maximal fluorescence observed with all 12 locations uncaged asynchronously, and compared the peak amplitude of the calcium transients as an increasing number of locations were uncaged near-synchronously (Fig. 2d). This revealed an abrupt deviation from the interpolated line at 6 locations uncaged, with a further increase as more locations were uncaged, before the observed response reached a plateau.

We repeated the quantification of dendritic nonlinearity in a sample of neurogliaform NDNF+ interneurons studied in the same way. These exhibited robust supralinear dendritic integration of uEPSPs (Fig 3 a-d). In keeping with the data from the sample neuron (Fig. 1) the degree of voltage nonlinearity was more marked for the integral (AUC) than for the peak amplitude, consistent with the activation of slow and/or regenerating conductances. As for dendritic calcium transients, 6 out of 7 interneurons exhibited a greater than predicted Fluo-4 fluorescence transient, implying supralinear summation (Fig. 3e, f).

Previous studies on dendritic integration have generally examined either voltage or dendritic calcium signalling in isolation, with the exception of an investigation of cerebellar layer molecular interneurons, which reported a striking dissociation, where calcium signalling exhibited supralinear summation while voltage summation was sublinear[19], contrasting with the present results. A parsimonious explanation for our findings is that dendritic regenerative currents are calcium-permeable, and that the calcium supralinearity is causally downstream from the voltage supralinearity. This principle was supported by the similar sigmoid shapes of the observed near-synchronous uEPSP amplitudes and calcium transients in the cell illustrated in Figs. 1 and 2. In another sample neuron which exhibited a prominent plateau potential upon near-synchronous uncaging at 6 or more locations, the peak calcium transient was proportional to the uEPSP AUC (Fig. 4h).

The asynchronous separate response baseline amplitude and AUC, as well as the distance along the dendrite from the soma to the uncaging location and the dendritic order of the stimulated dendrites are summarised in Supplementary Fig. 1.

Several conductances have been implicated in supralinear integration in principal neuron dendrites, including NMDARs[16-19,21-27], sodium channels[20,21,24,25,27,28] and calcium channels[19,21,25,27]. We asked whether they have similar roles in neurogliaform cells.

In a subset of cells reported in Fig. 3, we applied the NMDAR antagonist D-AP5 by bath perfusion. This robustly decreased both the uEPSP (Fig 5a) and the dendritic calcium transient amplitudes (Fig 5b) elicited with near-synchronous glutamate uncaging (see Fig. 5c-h for group averages). Summation of somatic uEPSPs and dendritic calcium transients became sublinear. This is consistent with the behaviour of a passive dendrite where the local synaptic driving force diminishes with depolarization.

In contrast to the effect of NMDAR blockade, dendritic integration of uEPSPs was only weakly affected by blocking L-type voltage-dependent calcium channels with nimodipine (Fig. 6), with some neurons continuing to exhibit supralinearity (e.g. Fig. 6a). Dendritic calcium supralinearity was however abolished (Fig. 6b, e). A caveat is that the dataset was obtained without pre-nimodipine baseline measurements. We tentatively conclude that L-type calcium channels have a much smaller contribution to voltage supralinearity than NMDARs, but contribute substantially to dendritic calcium influx.

We next examined the role of voltage-gated sodium channels by repeating the study in the continuous presence of tetrodotoxin (TTX). In a representative cell, robust supralinear integration was seen for both uEPSPs (Fig. 7a) and calcium fluorescence transients (Fig. 7b). Across all dendrites tested (n = 7), both the uEPSP and the dendritic calcium transient amplitudes summated supralinearity (Fig. 7c-h), with effect sizes

closely resembling those observed in the drug-free condition (Fig. 3). The data argue against a contribution of voltage-gated sodium channels to supralinear dendritic integration in NDNF+ neurogliaform interneurons.

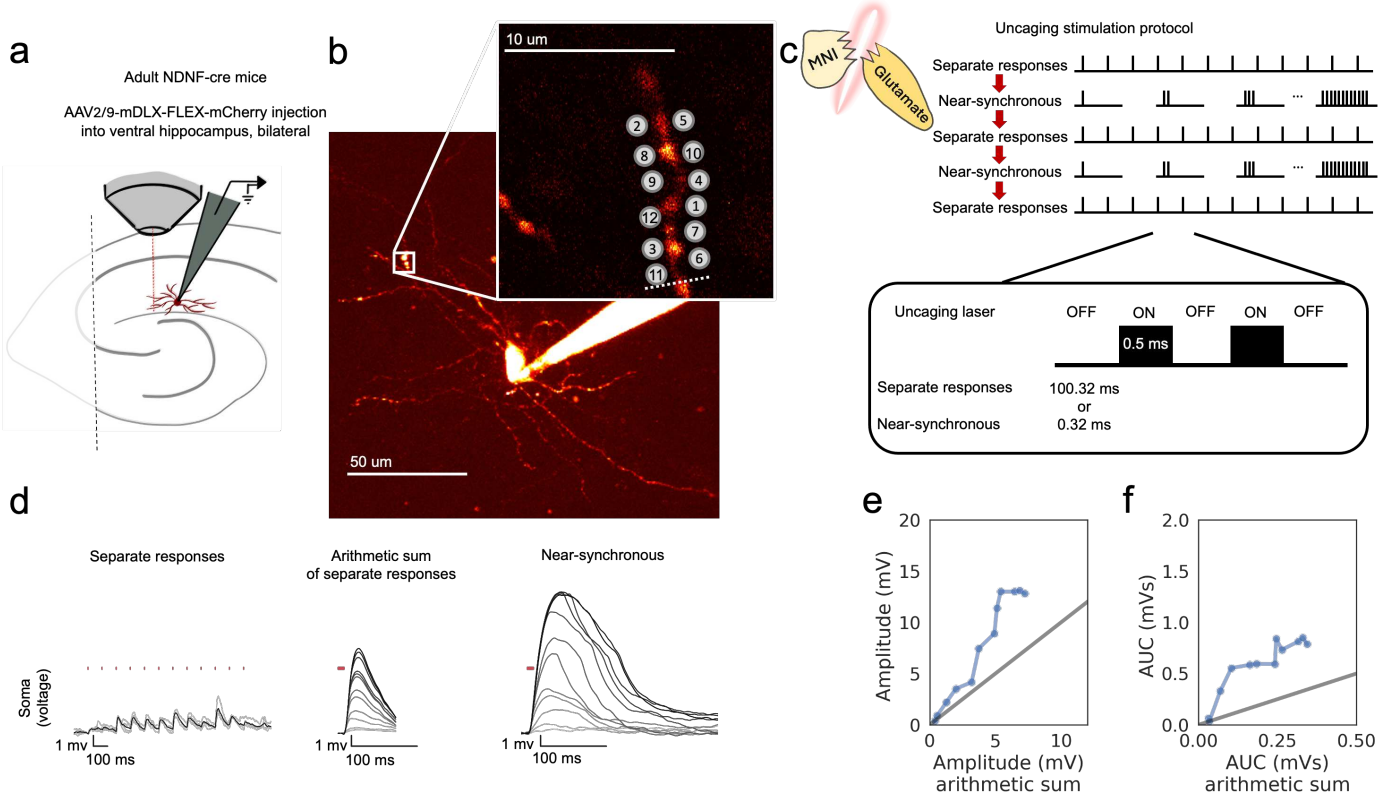

Fig 1. Experimental overview and representative example showing supralinear dendritic integration in a neurogliaform interneuron.

(a) Summary depicting the mouse model, viral expression, and acute slice preparation with patch-clamp and imaging and uncaging.

(b) Alexa-594 fluorescence Z-stack of a representative neurogliaform NDNF+ interneuron, with uncaging locations (inset). The image was obtained after the experiment was concluded.

(c) Uncaging protocol for asynchronous (separate responses) and near-synchronous conditions.

(d) Representative somatic voltage traces across asynchronous separate response and near-synchronous conditions. Laser uncaging light stimuli are indicated by red dots above the traces. uEPSPs were elicited in the asynchronous condition with light pulses separated by an interval of 100.32 ms (left; grey traces: individual sweeps; black traces average). The arithmetic sum traces were calculated by aligning and summing an increasing number of asynchronously evoked responses (middle). Near-synchronous uEPSPs were elicited with light pulses separated by an interval of 0.32 ms (right). The families of traces for the arithmetic sum and near-synchronously evoked responses are shown as light to dark grey traces, indicating an increase in the number of uncaging loci from 1 to 12).

(e) Peak amplitude of the recorded near-synchronous response plotted against the amplitude of the arithmetic sum as the number of uncaging loci was increased.

(f) Time integral of the recorded near-synchronous response (area under the curve, AUC) plotted against AUC of the arithmetic sum.

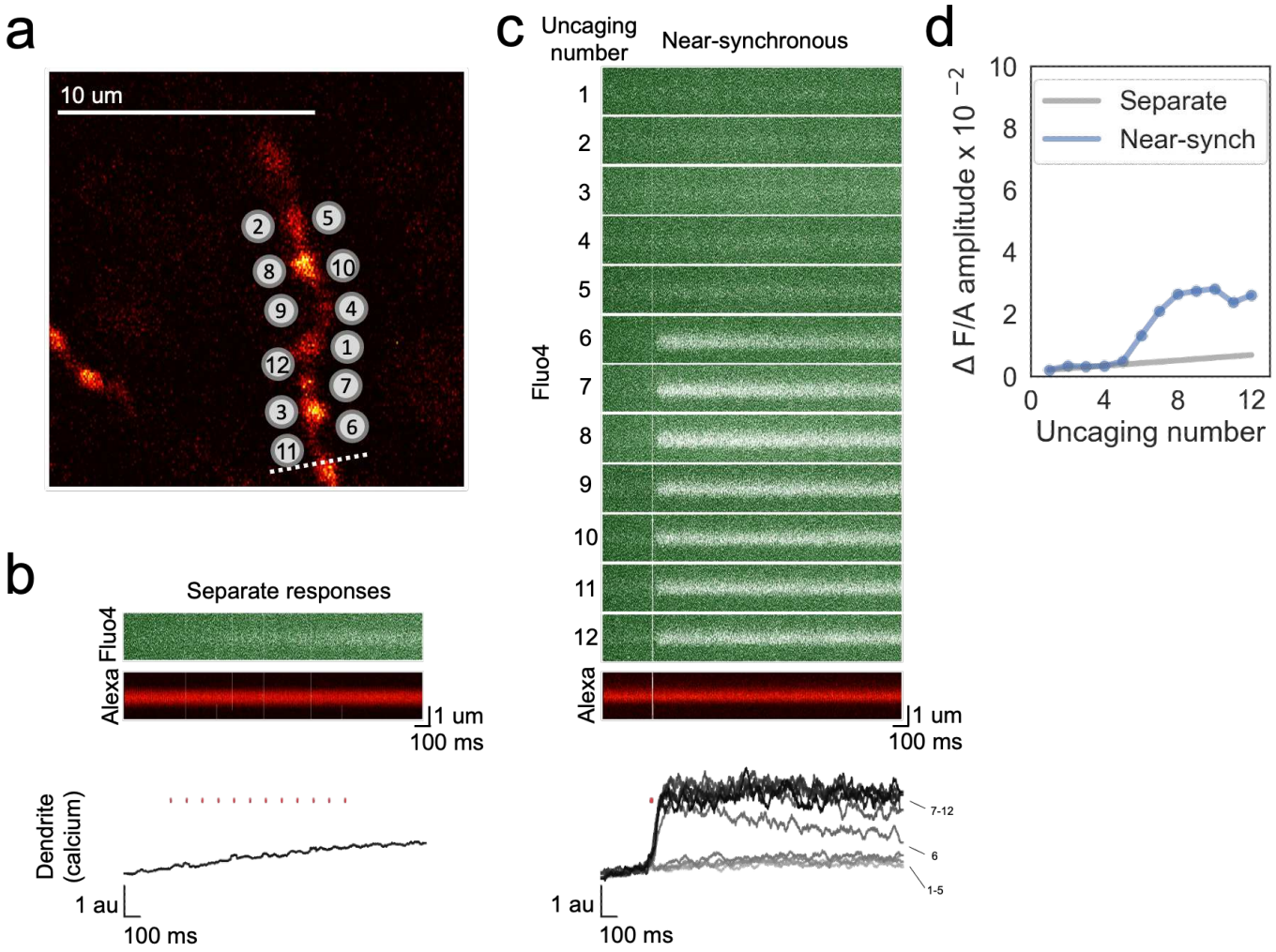

Fig. 2. Representative example of dendritic calcium fluorescence.

(a) Alexa-594 fluorescence framescan (same as Fig. 1a) showing uncaging locations and the position of the linescan used to measure dendritic calcium transients (dotted white line).

(b) Fluo-4 and Alexa-594 linescans during asynchronous sequential uncaging at 12 loci at times indicated by the vertical red dashes. The ratio of dendritic Fluo-4 to Alexa fluorescence is shown below (au: arbitrary unit).

(c) Linescans during near-synchronous uncaging at increasing numbers of locations (1 – 12, top to bottom).

(d) Fluo-4 fluorescence transient amplitude, normalised by Alexa-594 fluorescence, plotted against the number of locations uncaged near-synchronously. The grey line indicates the estimated separate response amplitude interpolated from the fluorescence measured between 1 and 12 locations uncaged asynchronously (see Methods).

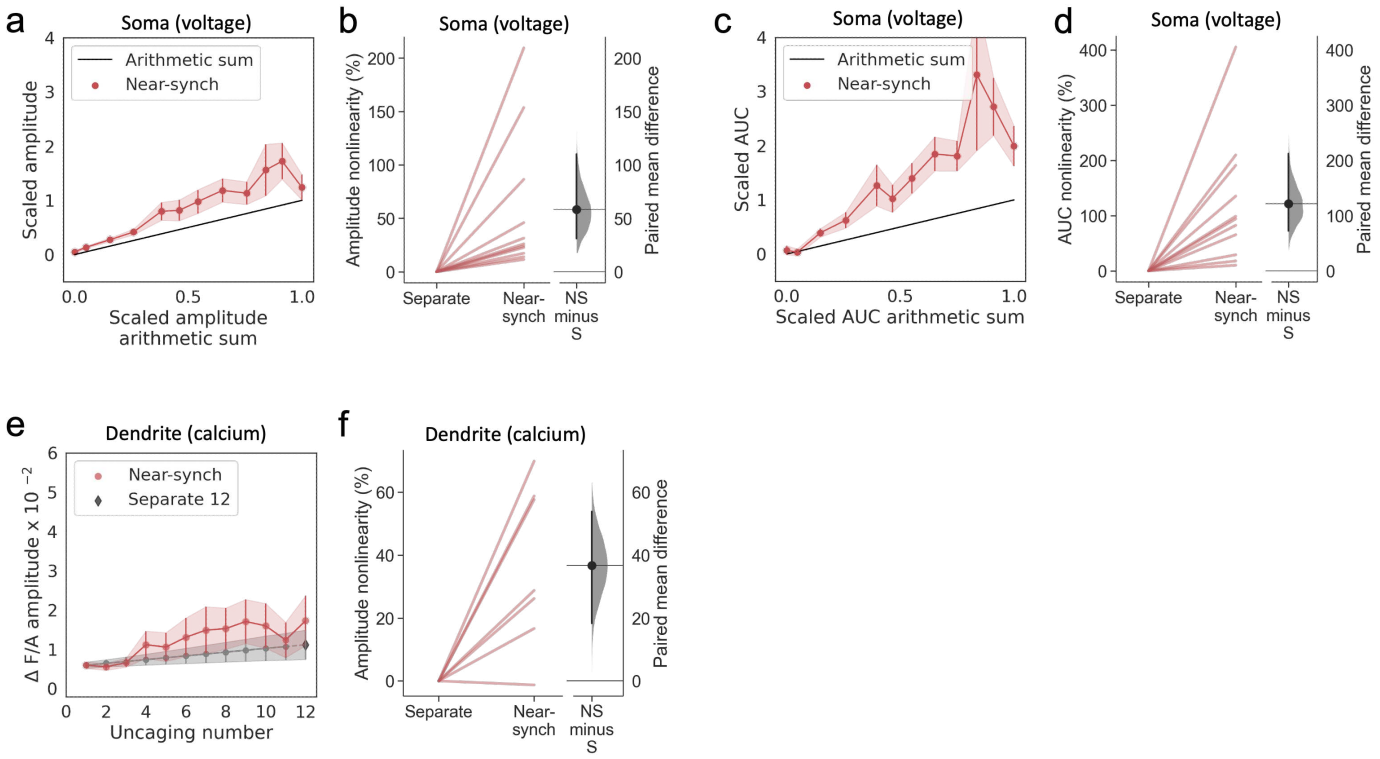

Fig. 3. Summary of supralinear dendritic integration in neurogliaform interneurons.

(a) Average scaled amplitude of recorded near-synchronous uEPSPs plotted against scaled amplitude of the arithmetic sum of asynchronously evoked uEPSPs as the cumulative number of uncaging locations was increased (n=11 dendrites in 11 cells from 9 animals; error bars represent SEM). Horizontal error bars for scaled amplitude of individual asynchronously evoked uEPSPs are omitted for clarity.

(b) Amplitude nonlinearity quantified for data shown in (a). The paired mean difference between near-synchronous (NS) and asynchronous separate responses (S) is 56% [95.0%CI 27%, 108%]. P<0.001 (two-sided permutation t-test compared to 0%).

(c) Average scaled near-synchronous uEPSP AUC plotted against scaled arithmetic sum of asynchronous separate responses, for the same dataset.

(d) AUC nonlinearity corresponding to panel (c). The paired mean difference between near-synchronous (NS) and asynchronous separate responses (S) is 122% [95.0%CI 73%, 213%]. P<0.001 (two-sided permutation t-test compared to 0%).

(e) Average Fluo-4/Alexa-594 fluorescence transients plotted against the cumulative number of uncaging locations. The grey line indicates the interpolated values used in the nonlinearity calculation (see Methods). The dark grey diamond indicates the amplitude from the 12^{th} asynchronous response. (n = 7 dendrites in 7 cells from 7 animals).

(f) Amplitude nonlinearity corresponding to panel (c) (dendritic calcium). The paired mean difference between near-synchronous (NS) and asynchronous separate responses (S) is 37% [95.0%CI 18%, 54%]. P=0.0138 (two-sided permutation t-test compared to 0%).

For the slopegraphs and Gardner-Altman estimation plots, paired observations are connected by coloured lines. The paired mean differences between the near-synchronous (NS) and asynchronous separate response (S) groups are shown in Gardner-Altman estimation plots as bootstrap sampling distributions. The mean differences are depicted as black dots. The 95% confidence intervals are indicated by the ends of the vertical error bars.

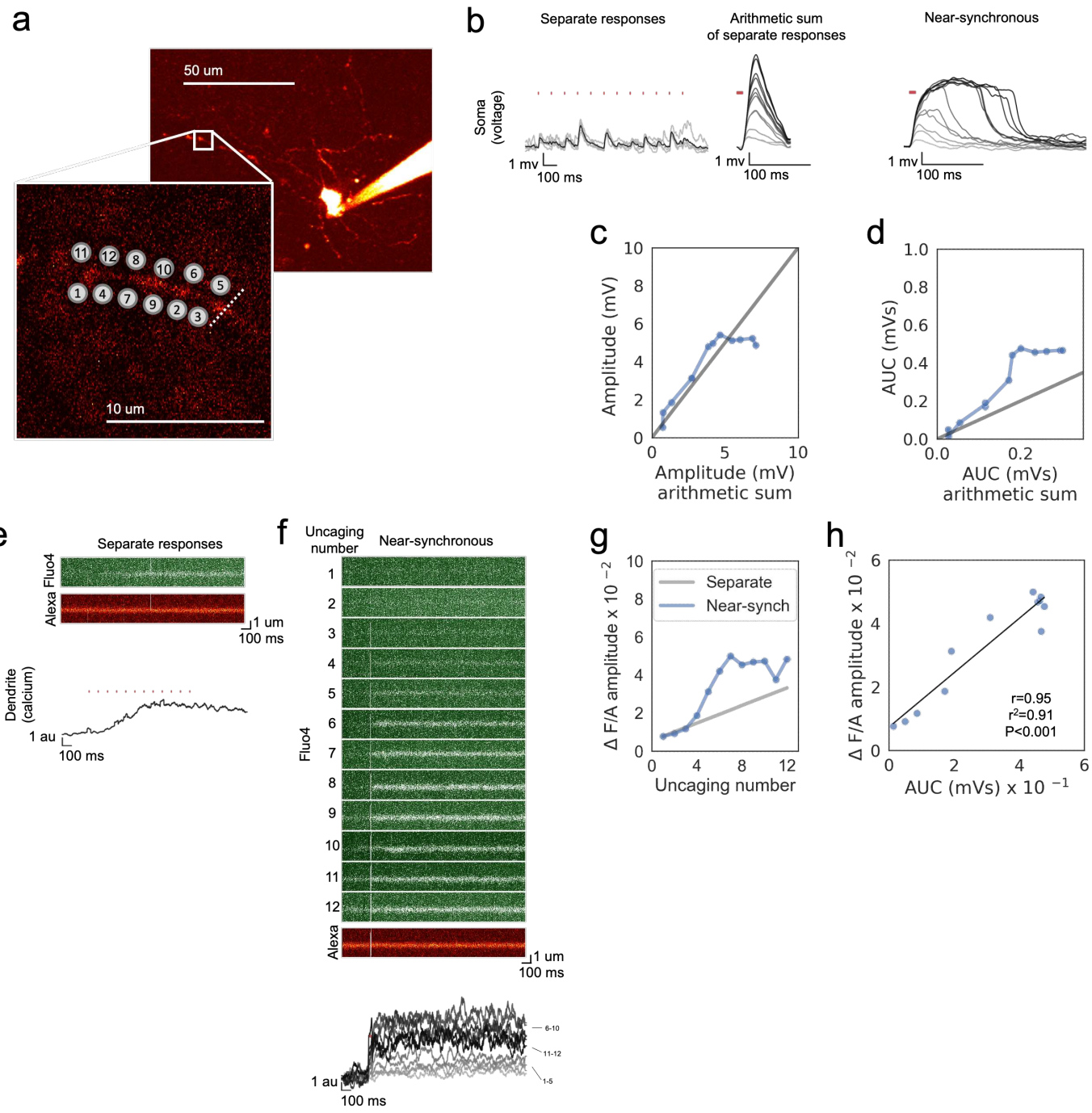

Fig. 4. Comparison of uEPSP time-integral and dendritic calcium in a neurogliaform cell.

(a) Alexa-594 fluorescence Z-stack, with uncaging locations and linescan position (inset).

(b) Somatic voltage traces across asynchronous separate response and near-synchronous conditions, with times of uncaging stimuli indicated by red dots). In the asynchronous condition, individual traces are shown in grey, and the average shown in black. For the near-synchronous traces, light to dark traces indicate responses as the numbers of near-synchronous uncaging stimuli was increased from 1 to 12. The arithmetic sum traces are indicated in the same way.

(c) Peak amplitude of the recorded near-synchronous response plotted against the amplitude of the arithmetic sum for increasing numbers of uncaging locations.

(d) Area under the curve (AUC) of the recorded near-synchronous response plotted against AUC of the arithmetic sum.

(e) Fluo-4 linescans in response to asynchronous stimulation. Locations 1 – 12 were sequentially stimulated at times indicated by red dots.

(f) Fluo-4 linescan in response to near-synchronous stimulation of increasing numbers of locations. The Fluo-4 fluorescence change from baseline was normalised to the fluorescence of the inert morphological dye Alexa-594 (the average linescan for Alexa-594 is shown beneath). Laser uncaging stimuli are indicated by red dots above the traces. Ratiometric calcium traces use arbitrary units (au).

(g) Fluo-4 fluorescence transient amplitude, normalised by Alexa-594 fluorescence, showing a deviation from the predicted response to asynchronous stimulation when more than 4 locations were uncaged near-synchronously. Grey line indicates the estimated asynchronous response amplitude using interpolated values (see methods).

(h) Fluo-4 fluorescence transient (normalised to Alexa-594 fluorescence plotted against uEPSP integral (AUC).

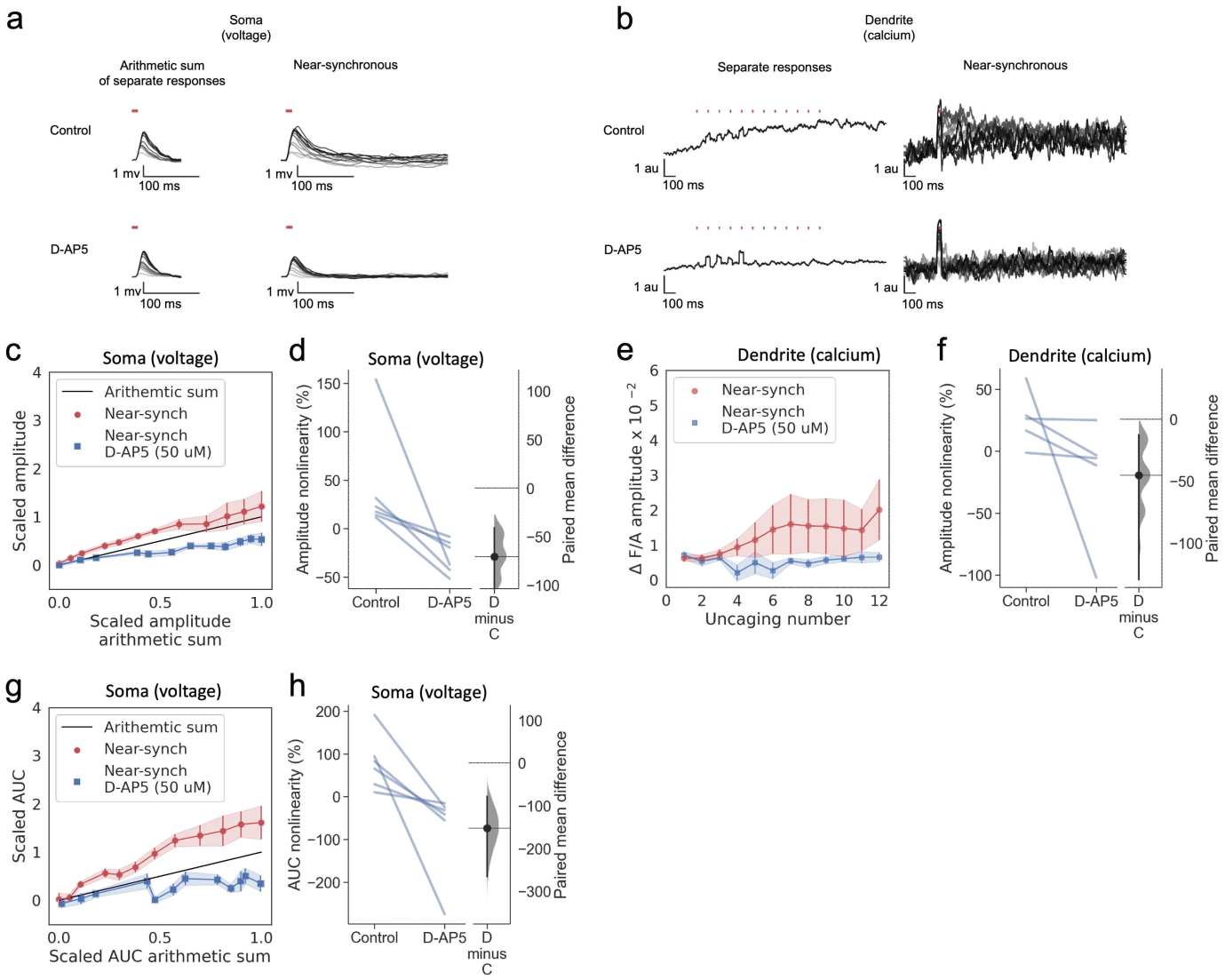

Fig. 5. Sublinear dendritic integration in neurogliaform interneurons with NMDARs blocked.

(a) Representative somatic voltage traces before (top) and after (bottom) D-AP5 (50 uM) perfusion in a representative example neuron. Uncaging protocol and data representation as in Figs. 1-3.

(b) Dendritic Fluo-4 traces in the same neuron, in response to asynchronous and near-synchronous uncaging, before (left) and after NMDAR blockade (right). Bleed-through of the uncaging laser is visible in some traces.

(c) Scaled amplitude of the recorded near-synchronous uEPSP plotted against scaled amplitude of the arithmetic sum, as the number of uncaging locations was increased. Error bars: SEM (n=6 dendrites in 6 cells from 6 animals). The supralinear relationship became sublinear with NMDARs blocked.

(d) Amplitude nonlinearity for individual neurons shown in (c) before and after D-AP5 perfusion. The paired mean difference between the two conditions is -71% [95.0%CI -147%, -41%]. P<0.001 (two-sided permutation t-test).

(e) Fluo-4 fluorescence transients (normalised to Alexa-594) plotted against the cumulative number of uncaging locations, before and after NMDAR blockade. Data plotted as in Fig. 2.

(f) Amplitude nonlinearity corresponding to panel (e). The paired mean difference between baseline and D-AP5 conditions is -45% [95.0%CI -129%, -13%]. P<0.001 (two-sided permutation t-test).

(g) Scaled time-integral of uEPSPs (AUC) plotted against scaled AUC arithmetic sum of asynchronous separate responses, before and after NMDAR blockade.

(h) AUC nonlinearity corresponding to panel (g). The paired mean difference between baseline and D-AP5 conditions is -140% [95.0%CI -307%, 65%]. P <0.001 (two-sided permutation t-test).

Slopegraphs and Gardner-Altman estimation plots as in Fig. 3.

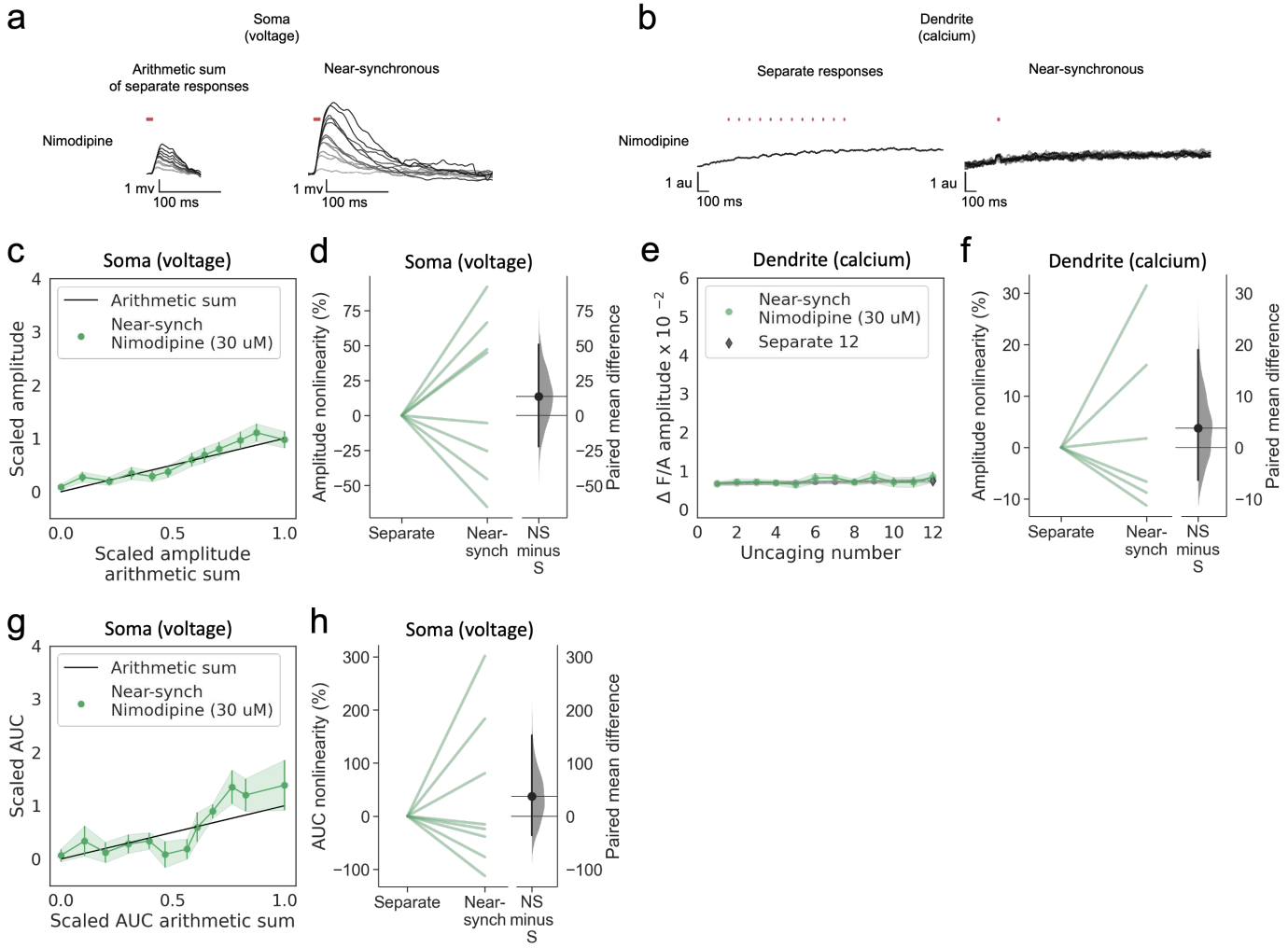

Fig. 6. L-type voltage-dependent calcium channel blockade abolishes nonlinear dendritic calcium summation.

(a) Somatic uEPSPs evoked by glutamate uncaging in one neuron in the presence of nimodipine (30 uM), showing supralinear uEPSP integration.

(b) Dendritic Fluo-4 fluorescence transients in the same neuron, showing absence of supralinear integration.

(c) Average scaled amplitude of the recorded near-synchronous uEPSP plotted against the arithmetic sum of the scaled asynchronous uEPSPs, as the cumulative number of uncaging locations was increased. Error bars show SEM (n=8 dendrites in 5 cells from 3 animals).

(d) Amplitude nonlinearity corresponding to (c). The paired mean difference between near-synchronous (NS) and asynchronous separate responses (S) is 14% [95.0%CI -22%, 51%]. P= 0.505 (two-sided permutation t-test compared to 0%).

(e) Fluo-4 fluorescence transient amplitude (normalised to Alexa-594) plotted against cumulative number of uncaging locations. Data plotted as in Fig. 2.

(f) Amplitude nonlinearity corresponding to (e). The paired mean difference between near-synchronous (NS) and asynchronous separate responses (S) is 4% [95.0%CI -6%, 19%]. P=0.561 (two-sided permutation t-test compared to 0%).

(g) uEPSP amplitude nonlinearity quantified by AUC, plotted in the same way as (c).

(h) AUC nonlinearity corresponding to (g). The paired mean difference between near-synchronous (NS) and asynchronous separate responses (S) is 37% [95.0%CI -37%, 153%]. P=0.497 (two-sided permutation t-test compared to 0%).

Slopegraphs and Gardner-Altman estimation plots as in Fig. 3.

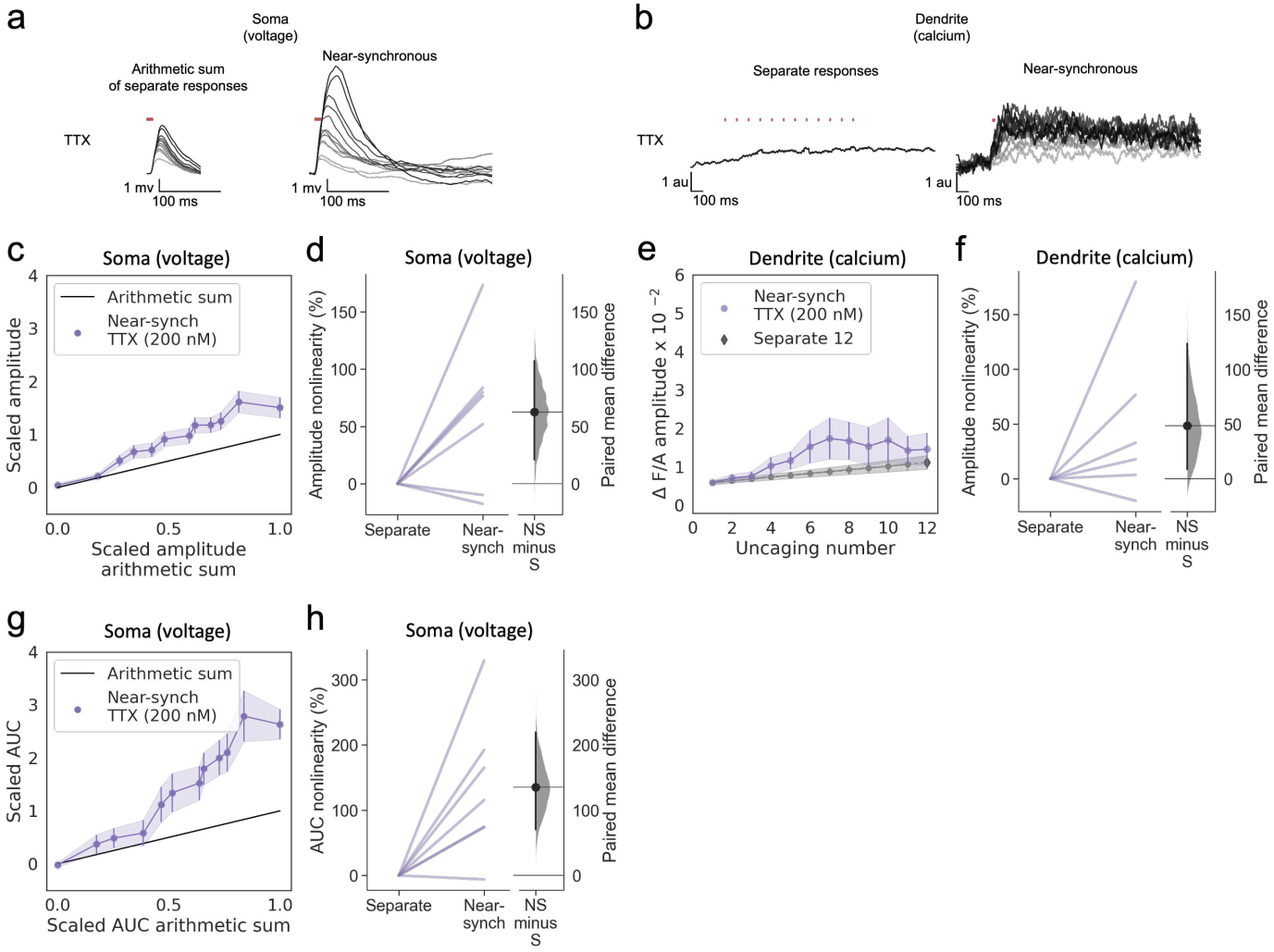

Fig. 7. Supralinear dendritic integration in neurogliaform interneurons does not require voltage-dependent sodium channels.

(a) Somatic uEPSPs evoked by uncaging glutamate in a representative neuron in the presence of TTX (200 nM), showing supralinear summation.

(b) Dendritic Fluo-4 fluorescence responses in the same neuron, showing supralinear calcium signalling.

(c) Average scaled amplitude of recorded near-synchronous uEPSP plotted against scaled amplitude arithmetic sum with increasing numbers of cumulative uncaging locations (n=7 dendrites in 5 cells from 5 animals).

(d) Amplitude nonlinearity corresponding to panel (c). The paired mean difference between near-synchronous (NS) and asynchronous separate responses (S) is 63% [95.0%CI 21%, 107%]. P=0.0382 (two-sided permutation t-test compared to 0%).

(e) Fluo-4 fluorescence transient amplitude (normalised to Alexa-594) plotted against the cumulative number of uncaging locations. Data plotted as in Fig. 2.

(f) Amplitude nonlinearity corresponding to panel (e). The paired mean difference between near-synchronous (NS) and asynchronous separate responses (S) is 48% [95.0%CI 9%, 123%]. P=0.088 (two-sided permutation t-test compared to 0%).

(g) uEPSP amplitude nonlinearity quantified by AUC, plotted in the same way as (c).

(h) AUC nonlinearity corresponding to (g). The paired mean difference between near-synchronous (NS) and asynchronous separate responses (S) is 135% [95.0%CI 71%, 220%]. P=0.011 (two-sided permutation t-test compared to 0%).

Slopegraphs and Gardner-Altman estimation plots as in Fig. 3.

Discussion

The main result of the present study is that hippocampal neurogliaform NDNF+ interneurons exhibit robust NMDAR-dependent supralinear integration of dendritic uEPSPs recorded at the soma. Supralinear NMDAR-dependent integration was also observed with dendritic calcium fluorescence measurements. In contrast to principal neurons, voltage-gated sodium channels are not involved in either type of supralinearity. L-type voltage-gated calcium channels have a more subtle role, in that blockade abolishes dendritic calcium supralinearity but does not prevent uEPSP supralinearity. Taken together, the data are consistent with a model where dendritic NMDARs are recruited by clustered synaptic receptor activation, accounting for supralinear summation of uEPSPs recorded at the soma, with L-type voltage-gated calcium channels acting downstream of dendritic depolarization and contributing to local calcium influx, but only to a small extent to uEPSPs at the soma.

The dependence of supralinear dendritic summation on NMDARs but not voltage-gated sodium channels is reminiscent to the pattern observed at dendrites of parvalbumin-positive interneurons in stratum[16]oriens. NMDARs have previously been implicated in synaptic signalling in neurogliaform cells[52,56,57] and also contribute to long-term potentiation[53].

The present study highlights the ability of neurogliaform neurons to perform local computations upstream of the site of axonal action potential initiation. The adaptive significance of this phenomenon remains to be determined. In principal neurons, synaptic inputs converging to common dendritic domains have been shown to exhibit correlated activity[58-60]. Synaptically evoked calcium transients in dendritic domains of interneurons of the visual cortex have also been reported to exhibit orientation tuning that is not apparent in the global activity recorded at the soma[55]. The dendritic nonlinearities uncovered by the present study, together with different forms of synaptic plasticity described in interneurons[61], are a candidate mechanism to achieve such an organization of information processing.

Material and methods

Animal and husbandry

Adult male and female mice of varying ages were throughout the study (ages 1-3 months). Transgenic mouse lines were maintained as heterozygotes. NDNF-cre+/+ or NDNF-cre+/- mice (The Jackson Laboratory B6.Cg-Ndnftm1.1(folA/cre)Hze/J; Stock No: 028536; Bar Harbor, ME, USA), bred on a C57BL/6 background) were used to target neurogliaform interneurons[62]. Animals were group-housed under a normal 12 h light/dark cycle. Cages were enriched with paper bedding, cardboard tube, plastic tube, and wooden chewing blocks. Mice had had unlimited access to standard laboratory chow and water. All procedures were carried out in accordance with the UK Animals (Scientific Procedures) Act, 1986.

Surgery for viral injection

Mice of at least 6 weeks of age were anaesthetised with isoflurane and placed into a stereotaxic frame, onto a heating pad to maintain body temperature. Mice were given Metacam (0.1 mg/kg) and buprenorphine (0.02 mg/kg) subcutaneously. Bilateral craniotomies were performed, positioned 3.1 mm caudal and ±3.12 mm lateral of Bregma. Virus (AAV2/9-mDlx-FLEX-mCherry; titre >10^{12} viral genomes/ml; VectorBuilder (Chicago, IL, USA)) was injected into the ventral CA1 region of both hippocampi using a Hamilton syringe 2.5 mm deep from the pia. 150 nL of virus was injected at each site at a rate of 100 nL/min. The needle was left in place for 5 min following injections before withdrawal. Mice were given 0.5 mL saline subcutaneously post-operatively to help with recovery and were monitored for 5 days following the procedure. Mice were sacrificed for experiments after a minimum of 3 weeks post-surgery.

Brain Slice preparation

Mice were sacrificed, the brains removed, and hippocampi dissected and sliced in ice-cold sucrose-based solution containing (in mM): 205 Sucrose, 10 Glucose, 26 NaHCO3, 2.5 KCl, 1.25 NaH2PO4, 0.5 CaCl2, 5 MgSO4, saturated with 95% O2 and 5% CO2. Transverse 400 µm hippocampal slices were cut using a Leica VT1200S vibrating microtome. Slices were incubated in artificial cerebrospinal fluid (aCSF) at 35 °C for 30 min and then at room temperature for 30 min. aCSF contained (in mM): mM: 124 NaCl, 3 KCl, 24 NaHCO3, 1.25 NaH2PO4 10 Glucose, 2.5 CaCl2, 1.3 MgSO4, saturated with 95% O2 and 5% CO2. The CA3 area was removed prior to slice transfer into the recording chamber to prevent recurrent activity.

Electrophysiology

The recording chamber was perfused with oxygenated aCSF maintained at 32 °C. Slices were first visualised using Dodt illumination on an Olympus FV1000 BX61 microscope. Fluorescent cells were identified in the CA1 stratum lacunosum/moleculare (neurogliaform cells) using Xcite epifluorescence. Borosilicate glass pipettes (pipette resistance of 4-5 MΩ) were pulled using a horizontal P2000 Sutter-instruments puller. The internal solution contained (in mM) 120 KMeSO3, 8 NaCl, 10 HEPES, 4 Mg-ATP, 0.3 Na-GTP, 10 KCl, ~295 mOsm, 7.4 pH. EGTA was not added to avoid introducing excess calcium buffering capacity. Internal solution aliquots were filtered on the day of experiment and small volumes of Alexa Fluor-594 (final concentration 50 µM) and Fluo-4 (final concentration 400 µM) solution aliquots were

added. Recordings were obtained using a Multiclamp 700B Molecular Devices amplifier filtered at 10 kHz and digitized at 20 kHz (National Instruments PCI-6221). WinWCP 5.5.6 (John Dempster, University of Strathclyde) software was used for data acquisition. After whole-cell break-in in V-clamp, the cells were switched to I=0 mode briefly to measure the resting membrane potential, before switching to I-clamp mode for experiments. All experiments were performed in I-clamp mode, with current continuously injected to maintain cell membrane between at ~−65 mV (0 to -50 pA). All data are presented without adjustment for the junction potential (~−15 mV). Recordings were discarded if they had an access resistance >25 MΩ and if access or input resistance changed by >20% over the course of the experiment. All experiments were conducted in the presence of picrotoxin 50 µM and CGP55845 1µM to block GABAergic transmission. D-AP5 (50 µM), tetrodotoxin (200 nM), nimodipine (30 µM) were bath-applied to block NMDARs, voltage-activated sodium channels, or L-type calcium channels respectively. D-AP5 was applied over a period of 7 minutes following a control recording, whilst tetrodotoxin (TTX) and nimodipine were present in the recording chamber throughout their respective experiments.

Two-photon imaging and uncaging

Simultaneous two-photon imaging and uncaging of MNI-caged glutamate were performed using two Ti-sapphire lasers tuned to 810 nm and 720 nm, for imaging and uncaging respectively (Mai-Tai, Spectra Physics; Chameleon, Coherent). MNI-caged-glutamate (3 mM; Hello Bio) was added to the aCSF in a closed recirculating system upon patch-clamp break-in. 12 uncaging locations ~2 µm apart and <1 µm away from the dendrite were chosen on either side of second-order dendrites in pseudo-random patterns. 0.5 ms-long pulses of 720 nm light were used to uncage MNI-caged-glutamate. The uncaging light pulses were separated by either 100.32 ms or 0.32 ms in the control asynchronous (separate responses) or the near-synchronous protocols respectively. In the near-synchronous protocol, increasing numbers of uncaging locations were activated in a cumulative manner across sweeps 1 to 12. Inter-sweep interval was >30 s, during which adjustments were made to account for any focal and x-y drift. Cycles of control asynchronous and near-synchronous stimulation protocols were done one after the other to produce mean responses, without changing the order of dendritic locations uncaged. Uncaging times and locations were controlled by scanning software (Fluoview 1000V) and a pulse generator (Berkeley Nucleonics) with a Pockels cell. Calcium signals were acquired using 810 nM laser light, linescanning on the same dendritic branch as the uncaging and down-stream of the uncaging locations toward the soma. Cells were discarded upon observation of photodamage or upon change in resting membrane potential of >10 mV. All z-stacks used for the analysis of morphology and example figures were captured at the end of experiments to maximise the amount of time for experiments before cell health deterioration. Photomultiplier tube filters used: 515–560 nm (Fluo-4); 590–650 nm (Alexa-594).

Quantification and statistical analyses

Area under the curve and amplitude nonlinearity was regarded as the primary experimental outcome.

Response nonlinearity was quantified using the following equation[16]

$$\%\ nonlinearity = \sum_{i=2}^{n} \frac{\frac{Mi}{Ai} - 1}{n-1} * 100\%$$

Mi amplitude of the ith measured uEPSP (composed of i individual uncaging spots)

Ai amplitude of the ith constructed arithmetically summed uEPSP

n is the total number of uncaging locations.

Seeing as the calcium signal did not return to its pre-stimulation baseline in between flashes of uncaging laser light in the control asynchronous (separate responses) condition, calculating the arithmetic sum of individual responses was not possible. Therefore, to obtain an estimate of nonlinearity for calcium traces, values from linear interpolation were used. The first sweep of the test condition, where only a single location was stimulated using uncaging light, was treated as the first value of the control asynchronous (separate responses) condition for the purposes of interpolation. The second and final value used for interpolation was from the end of the control (separate responses) trace, so that the signal would encompass all 12 uncaging events.

Calcium signals were quantified using the following equation:

$$\Delta F/A$$

ΔF relative change in the Fluo-4 green channel fluorescence from baseline

A Alexa-594 red channel fluorescence

Traces including action potentials were excluded from analysis. Traces were filtered using a Savitzky-Golay filter. Due to the substantial variabiity in responses across dendrites, dendrites were used as the experimental unit. No cell had more than 2 dendrites investigated. The numbers of dendrites, cells, and animals are reported in figure legends. α = 0.05 was applied for all statistical tests. The degrees of freedom, t, and p values are presented in the figure legends and discussed in text, as appropriate. Estimation statistics[65] and the generation of slopegraphs and Gardner-Altman estimation plots were performed using code provided by Ho et al. (2019)[66]. 95% confidence intervals of the mean difference were calculated by bootstrap resampling with 5000 resamples. The confidence interval is bias-corrected and accelerated. P values are provided with estimation statistics for legacy purposes only. Data were processed using custom Python code, Microsoft Excel, and WinWCP 5.5.6 (John Dempster, University of Strathclyde). Figures created using custom Python code, Microsoft PowerPoint, Procreate.

References

1. Makarov R, Pagkalos M, Poirazi P. Dendrites and efficiency: Optimizing performance and resource utilization. *Curr Opin Neurobiol*. Dec 2023;83:102812. doi:10.1016/j.conb.2023.102812
2. Mikulasch FA, Rudelt L, Wibral M, Priesemann V. Where is the error? Hierarchical predictive coding through dendritic error computation. *Trends Neurosci*. Jan 2023;46(1):45-59. doi:10.1016/j.tins.2022.09.007
3. Poirazi P, Papoutsi A. Illuminating dendritic function with computational models. *Nat Rev Neurosci*. Jun 2020;21(6):303-321. doi:10.1038/s41583-020-0301-7
4. Larkum ME, Wu J, Duverdin SA, Gidon A. The Guide to Dendritic Spikes of the Mammalian Cortex In Vitro and In Vivo. *Neuroscience*. May 1 2022;489:15-33. doi:10.1016/j.neuroscience.2022.02.009
5. Stuart GJ, Spruston N. Dendritic integration: 60 years of progress. *Nat Neurosci*. Dec 2015;18(12):1713-21. doi:10.1038/nn.4157
6. Tran-Van-Minh A, Caze RD, Abrahamsson T, Cathala L, Gutkin BS, DiGregorio DA. Contribution of sublinear and supralinear dendritic integration to neuronal computations. *Front Cell Neurosci*. 2015;9:67. doi:10.3389/fncel.2015.00067
7. Lorenzo J, Binczak S, Jacquir S. A multilayer-multiplexer network processing scheme based on the dendritic integration in a single neuron. *AIMS Neurosci*. 2022;9(1):76-113. doi:10.3934/Neuroscience.2022006
8. Kim YJ, Ujfalussy BB, Lengyel M. Parallel functional architectures within a single dendritic tree. *Cell Rep*. Apr 25 2023;42(4):112386. doi:10.1016/j.celrep.2023.112386
9. Ujfalussy BB, Makara JK, Lengyel M, Branco T. Global and Multiplexed Dendritic Computations under In Vivo-like Conditions. *Neuron*. Nov 7 2018;100(3):579-592 e5. doi:10.1016/j.neuron.2018.08.032
10. Beniaguev D, Segev I, London M. Single cortical neurons as deep artificial neural networks. *Neuron*. Sep 1 2021;109(17):2727-2739 e3. doi:10.1016/j.neuron.2021.07.002
11. Wybo WAM, Tsai MC, Tran VAK, et al. NMDA-driven dendritic modulation enables multitask representation learning in hierarchical sensory processing pathways. *Proc Natl Acad Sci U S A*. Aug 8 2023;120(32):e2300558120. doi:10.1073/pnas.2300558120
12. Poleg-Polsky A. Dendritic Spikes Expand the Range of Well Tolerated Population Noise Structures. *J Neurosci*. Nov 13 2019;39(46):9173-9184. doi:10.1523/JNEUROSCI.0638-19.2019
13. Leugering J, Nieters P, Pipa G. Dendritic plateau potentials can process spike sequences across multiple time-scales. *Frontiers in Cognition*. 2023;2doi:10.3389/fcogn.2023.1044216
14. Gidon A, Zolnik TA, Fidzinski P, et al. Dendritic action potentials and computation in human layer 2/3 cortical neurons. *Science*. 2020;367:83-87.
15. Magó A, Kis N, Lükő B, Makara JK. Distinct dendritic Ca2+ spike forms produce opposing input-output transformations in rat CA3 pyramidal cells. *elife*. 2021;10:e74493.
16. Cornford JH, Mercier MS, Leite M, Magloire V, Hausser M, Kullmann DM. Dendritic NMDA receptors in parvalbumin neurons enable strong and stable neuronal assemblies. *Elife*. Oct 28 2019;8doi:10.7554/eLife.49872
17. Larkum ME, Nevian T, Sandler M, Polsky A, Schiller J. Synaptic integration in tuft dendrites oflLayer 5 pyramidal neurons: a new unifying principle. *Science*. 2009;325(5941):756-760.
18. Katona G, Kaszas A, Turi GF, et al. Roller Coaster Scanning reveals spontaneous triggering of dendritic spikes in CA1 interneurons. *Proc Natl Acad Sci U S A*. Feb 1 2011;108(5):2148-53. doi:10.1073/pnas.1009270108
19. Tran-Van-Minh A, Abrahamsson T, Cathala L, DiGregorio DA. Differential Dendritic Integration of Synaptic Potentials and Calcium in Cerebellar Interneurons. *Neuron*. Aug 17 2016;91(4):837-850. doi:10.1016/j.neuron.2016.07.029
20. Masala N, Pofahl M, Haubrich AN, et al. Targeting aberrant dendritic integration to treat cognitive comorbidities of epilepsy. *Brain*. Jun 1 2023;146(6):2399-2417. doi:10.1093/brain/awac455
21. Chiovini B, Turi GF, Katona G, et al. Dendritic spikes induce ripples in parvalbumin interneurons during hippocampal sharp waves. *Neuron*. May 21 2014;82(4):908-24. doi:10.1016/j.neuron.2014.04.004
22. Testa-Silva G, Rosier M, Honnuraiah S, et al. High synaptic threshold for dendritic NMDA spike generation in human layer 2/3 pyramidal neurons. *Cell Rep*. Dec 13 2022;41(11):111787. doi:10.1016/j.celrep.2022.111787
23. Lafourcade M, van der Goes MH, Vardalaki D, et al. Differential dendritic integration of long-range inputs in association cortex via subcellular changes in synaptic AMPA-to-NMDA receptor ratio. *Neuron*. May 4 2022;110(9):1532-1546 e4. doi:10.1016/j.neuron.2022.01.025
24. Losonczy A, Magee JC. Integrative properties of radial oblique dendrites in hippocampal CA1 pyramidal neurons. *Neuron*. Apr 20 2006;50(2):291-307. doi:10.1016/j.neuron.2006.03.016
25. Camire O, Lazarevich I, Gilbert T, Topolnik L. Mechanisms of Supralinear Calcium Integration in Dendrites of Hippocampal CA1 Fast-Spiking Cells. *Front Synaptic Neurosci*. 2018;10:47. doi:10.3389/fnsyn.2018.00047

26. Camire O, Topolnik L. Dendritic calcium nonlinearities switch the direction of synaptic plasticity in fast-spiking interneurons. *J Neurosci*. Mar 12 2014;34(11):3864-77. doi:10.1523/JNEUROSCI.2253-13.2014
27. Branco T, Hausser M. Synaptic integration gradients in single cortical pyramidal cell dendrites. *Neuron*. Mar 10 2011;69(5):885-92. doi:10.1016/j.neuron.2011.02.006
28. Ariav G, Polsky A, Schiller J. Submillisecond precision of the input–output transformation function mediated by fast sodium dendritic spikes in basal dendrites of CA1 pyramidal neurons. *Neuroscience*. 2003;23(21):7750-7758.
29. Harnett MT, Xu NL, Magee JC, Williams SR. Potassium channels control the interaction between active dendritic integration compartments in layer 5 cortical pyramidal neurons. *Neuron*. Aug 7 2013;79(3):516-29. doi:10.1016/j.neuron.2013.06.005
30. Hoffman DA, Magee JC, Colbert CM, Johnston D. K+ channel regulation of signal propagation in dendrites of hippocampal pyramidal neurons. *Nature*. 1997;387:869-875.
31. Freund TF, Buzsáki G. Interneurons of the hippocampus. *Hippocampus*. 1998;6(4):347-470. doi:10.1002/(sici)1098-1063(1996)6:4<347::Aid-hipo1>3.0.Co;2-i
32. Hertag L, Sprekeler H. Learning prediction error neurons in a canonical interneuron circuit. *Elife*. Aug 21 2020;9doi:10.7554/eLife.57541
33. Tzilivaki A, Tukker JJ, Maier N, Poirazi P, Sammons RP, Schmitz D. Hippocampal GABAergic interneurons and memory. *Neuron*. Oct 18 2023;111(20):3154-3175. doi:10.1016/j.neuron.2023.06.016
34. Hu H, Vervaeke K. Synaptic integration in cortical inhibitory neuron dendrites. *Neuroscience*. Jan 1 2018;368:115-131. doi:10.1016/j.neuroscience.2017.06.065
35. Kriener B, Hu H, Vervaeke K. Parvalbumin interneuron dendrites enhance gamma oscillations. *Cell Rep*. Jun 14 2022;39(11):110948. doi:10.1016/j.celrep.2022.110948
36. Dinocourt C, Petanjek Z, Freund TF, Ben-Ari Y, Esclapez M. Loss of interneurons innervating pyramidal cell dendrites and axon initial segments in the CA1 region of the hippocampus following pilocarpine-induced seizures. *J Comp Neurol*. May 12 2003;459(4):407-25. doi:10.1002/cne.10622
37. Fujiwara-Tsukamoto Y, Isomura Y, Imanishi M, et al. Prototypic seizure activity driven by mature hippocampal fast-spiking interneurons. *J Neurosci*. Oct 13 2010;30(41):13679-89. doi:10.1523/JNEUROSCI.1523-10.2010
38. Magloire V, Mercier MS, Kullmann DM, Pavlov I. GABAergic Interneurons in Seizures: Investigating Causality With Optogenetics. *Neuroscientist*. Aug 2019;25(4):344-358. doi:10.1177/1073858418805002
39. Marx M, Haas CA, Haussler U. Differential vulnerability of interneurons in the epileptic hippocampus. *Front Cell Neurosci*. 2013;7:167. doi:10.3389/fncel.2013.00167
40. Belforte JE, Zsiros V, Sklar ER, et al. Postnatal NMDA receptor ablation in corticolimbic interneurons confers schizophrenia-like phenotypes. *Nat Neurosci*. Jan 2010;13(1):76-83. doi:10.1038/nn.2447
41. Jahangir M, Zhou JS, Lang B, Wang XP. GABAergic System Dysfunction and Challenges in Schizophrenia Research. *Front Cell Dev Biol*. 2021;9:663854. doi:10.3389/fcell.2021.663854
42. Marin O. Interneuron dysfunction in psychiatric disorders. *Nat Rev Neurosci*. Jan 18 2012;13(2):107-20. doi:10.1038/nrn3155
43. Lunden JW, Durens M, Phillips AW, Nestor MW. Cortical interneuron function in autism spectrum condition. *Pediatr Res*. Jan 2019;85(2):146-154. doi:10.1038/s41390-018-0214-6
44. Hijazi S, Heistek TS, Scheltens P, et al. Early restoration of parvalbumin interneuron activity prevents memory loss and network hyperexcitability in a mouse model of Alzheimer's disease. *Mol Psychiatry*. Dec 2020;25(12):3380-3398. doi:10.1038/s41380-019-0483-4
45. Verret L, Mann EO, Hang GB, et al. Inhibitory interneuron deficit links altered network activity and cognitive dysfunction in Alzheimer model. *Cell*. Apr 27 2012;149(3):708-21. doi:10.1016/j.cell.2012.02.046
46. Pelkey KA, Chittajallu R, Craig MT, Tricoire L, Wester JC, McBain CJ. Hippocampal GABAergic Inhibitory Interneurons. *Physiol Rev*. Oct 1 2017;97(4):1619-1747. doi:10.1152/physrev.00007.2017
47. Mitchell DE, Miranda-Rottmann S, Blanchard M, Araya R. Altered integration of excitatory inputs onto the basal dendrites of layer 5 pyramidal neurons in a mouse model of Fragile X syndrome. *Proc Natl Acad Sci U S A*. Jan 10 2023;120(2):e2208963120. doi:10.1073/pnas.2208963120
48. Griesius S, O'Donnell C, Waldron S, et al. Reduced expression of the psychiatric risk gene DLG2 (PSD93) impairs hippocampal synaptic integration and plasticity. *Neuropsychopharmacology*. Jun 2022;47(7):1367-1378. doi:10.1038/s41386-022-01277-6
49. Nelson AD, Bender KJ. Dendritic Integration Dysfunction in Neurodevelopmental Disorders. *Dev Neurosci*. 2021;43(3-4):201-221. doi:10.1159/000516657
50. Palmer LM. Dendritic integration in pyramidal neurons during network activity and disease. *Brain Res Bull*. Apr 2014;103:2-10. doi:10.1016/j.brainresbull.2013.09.010

51. Booker SA, Vida I. Morphological diversity and connectivity of hippocampal interneurons. *Cell Tissue Res*. Sep 2018;373(3):619-641. doi:10.1007/s00441-018-2882-2
52. Chittajallu R, Wester JC, Craig MT, et al. Afferent specific role of NMDA receptors for the circuit integration of hippocampal neurogliaform cells. *Nat Commun*. Jul 28 2017;8(1):152. doi:10.1038/s41467-017-00218-y
53. Mercier MS, Magloire V, Cornford JH, Kullmann DM. Long-term potentiation in neurogliaform interneurons modulates excitation-inhibition balance in the temporoammonic pathway. *J Physiol*. Sep 2022;600(17):4001-4017. doi:10.1113/JP282753
54. Tricoire L, Pelkey KA, Daw MI, et al. Common origins of hippocampal Ivy and nitric oxide synthase expressing neurogliaform cells. *J Neurosci*. Feb 10 2010;30(6):2165-76. doi:10.1523/JNEUROSCI.5123-09.2010
55. Chen TW, Wardill TJ, Sun Y, et al. Ultrasensitive fluorescent proteins for imaging neuronal activity. *Nature*. Jul 18 2013;499(7458):295-300. doi:10.1038/nature12354
56. Price CJ, Cauli B, Kovacs ER, et al. Neurogliaform neurons form a novel inhibitory network in the hippocampal CA1 area. *J Neurosci*. Jul 20 2005;25(29):6775-86. doi:10.1523/JNEUROSCI.1135-05.2005
57. Armstrong C, Szabadics J, Tamas G, Soltesz I. Neurogliaform cells in the molecular layer of the dentate gyrus as feed-forward gamma-aminobutyric acidergic modulators of entorhinal-hippocampal interplay. *J Comp Neurol*. Jun 1 2011;519(8):1476-91. doi:10.1002/cne.22577
58. Iacaruso MF, Gasler IT, Hofer SB. Synaptic organization of visual space in primary visual cortex. *Nature*. Jul 27 2017;547(7664):449-452. doi:10.1038/nature23019
59. Takahashi N, Kitamura K, Matsuo N, et al. Locally synchronized synaptic inputs. *Science*. Jan 20 2012;335(6066):353-6. doi:10.1126/science.1210362
60. Wilson DE, Whitney DE, Scholl B, Fitzpatrick D. Orientation selectivity and the functional clustering of synaptic inputs in primary visual cortex. *Nat Neurosci*. Aug 2016;19(8):1003-9. doi:10.1038/nn.4323
61. Kullmann DM, Moreau AW, Bakiri Y, Nicholson E. Plasticity of inhibition. *Neuron*. Sep 20 2012;75(6):951-62. doi:10.1016/j.neuron.2012.07.030
62. Tasic B, Menon V, Nguyen TN, et al. Adult mouse cortical cell taxonomy revealed by single cell transcriptomics. *Nat Neurosci*. Feb 2016;19(2):335-46. doi:10.1038/nn.4216
63. Taniguchi H, He M, Wu P, et al. A resource of Cre driver lines for genetic targeting of GABAergic neurons in cerebral cortex. *Neuron*. Sep 22 2011;71(6):995-1013. doi:10.1016/j.neuron.2011.07.026
64. Madisen L, Zwingman TA, Sunkin SM, et al. A robust and high-throughput Cre reporting and characterization system for the whole mouse brain. *Nat Neurosci*. Jan 2010;13(1):133-40. doi:10.1038/nn.2467
65. Claridge-Chang A, Assam PN. Estimation statistics should replace significance testing. *Nat Methods*. Feb 2016;13(2):108-9. doi:10.1038/nmeth.3729
66. Ho J, Tumkaya T, Aryal S, Choi H, Claridge-Chang A. Moving beyond P values: data analysis with estimation graphics. *Nat Methods*. Jul 2019;16(7):565-566. doi:10.1038/s41592-019-0470-3

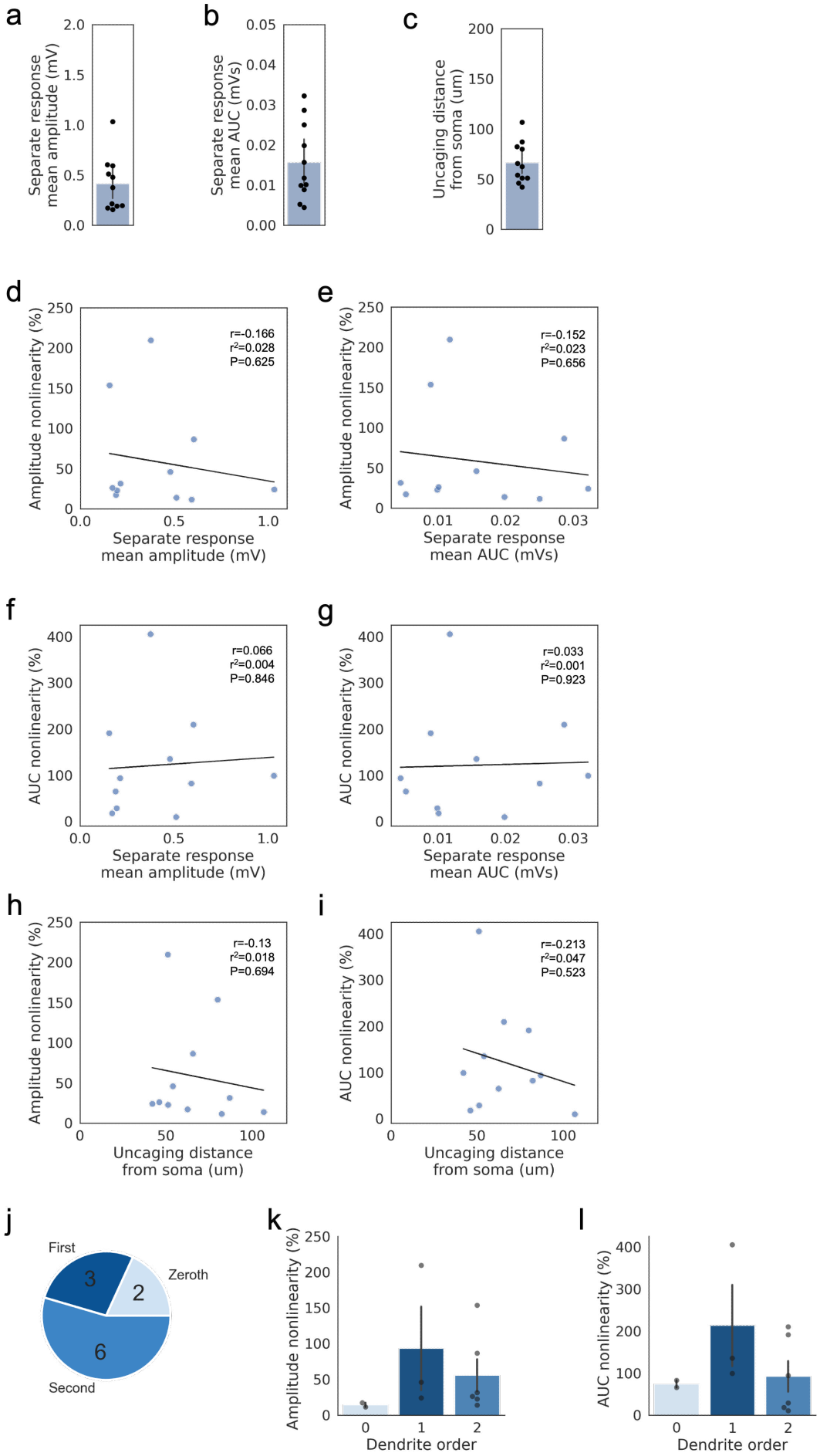

Supplementary Fig. 1. Relationships among uncaging parameters and uEPSP nonlinearity.

(a) Mean asynchronous separate response uEPSP amplitude.

(b) Mean asynchronous separate response uEPSP AUC.

(c) Distance from the soma to the uncaging location along the dendrite.

(d) Separate response mean amplitude plotted against amplitude nonlinearity following near-synchronous uncaging.

(e) Separate response mean area under the curve (AUC) plotted against amplitude nonlinearity following near-synchronous uncaging.

(f) Separate response mean amplitude plotted against AUC nonlinearity following near-synchronous uncaging.

(g) Separate response mean AUC plotted against AUC nonlinearity following near-synchronous uncaging.

(h) Uncaging distance from soma plotted against amplitude nonlinearity.

(i) Uncaging distance from soma plotted against AUC nonlinearity.

(j) Dendritic order for dendrites used for glutamate uncaging. The numbers in the pie chart represent the numbers of dendrites in the respective categories.

(k) Amplitude nonlinearity split by dendrite order.

(l) AUC nonlinearity split by dendrite order.

Linear regressions are depicted as black lines. Pearson correlation parameters depicted in correlation panels. Summary values are depicted as mean ± SEM. Voltage data: 9 animals, 11 cells, 11 dendritic locations